Corrected: Publisher correction

ARTICLE

A Co_3O_4-CDots-C_3N_4 three component electrocatalyst design concept for efficient and tunable CO_2 reduction to syngas

Sijie Guo[1], Siqi Zhao[1], Xiuqin Wu[1], Hao Li[1], Yunjie Zhou[1], Cheng Zhu[1], Nianjun Yang [2],
Xin Jiang[2], Jin Gao[1], Liang Bai[1], Yang Liu[1], Yeshayahu Lifshitz[1,3], Shuit-Tong Lee[1] & Zhenhui Kang[1]

Syngas, a CO and H_2 mixture mostly generated from non-renewable fossil fuels, is an essential feedstock for production of liquid fuels. Electrochemical reduction of CO_2 and H^+/H_2O is an alternative renewable route to produce syngas. Here we introduce the concept of coupling a hydrogen evolution reaction (HER) catalyst with a CDots/C_3N_4 composite (a CO_2 reduction catalyst) to achieve a cheap, stable, selective and efficient route for tunable syngas production. Co_3O_4, MoS_2, Au and Pt serve as the HER component. The Co_3O_4-CDots-C_3N_4 electrocatalyst is found to be the most efficient among the combinations studied. The H_2/CO ratio of the produced syngas is tunable from 0.07:1 to 4:1 by controlling the potential. This catalyst is highly stable for syngas generation (over 100 h) with no other products besides CO and H_2. Insight into the mechanisms balancing between CO_2 reduction and H_2 evolution when applying the HER-CDots-C_3N_4 catalyst concept is provided.

[1] Jiangsu Key Laboratory for Carbon-Based Functional Materials & Devices, Institute of Functional Nano & Soft Materials (FUNSOM), Soochow University, 199 Ren'ai Road, Suzhou 215123 Jiangsu, China. [2] Institute of Materials Engineering, University of Siegen, 57076 Siegen, Germany. [3] Department of Materials Science and Engineering, Technion, Israel Institute of Technology, Haifa 3200003, Israel. Correspondence and requests for materials should be addressed to X.J. (email: xin.jiang@uni-siegen.de) or to Y. Liu (email: yangl@suda.edu.cn) or to Y. Lifshitz (email: shayli@technion.ac.il) or to Z.K. (email: zhkang@suda.edu.cn)

Syngas, a mixture of H_2 and CO, is a critical feedstock for production of synthetic fuels and industrial chemicals via well-established industrial processes such as the Fischer–Tropsch process (commercialized by Sasol and Shell)[1, 2]. The H_2/CO ratio in syngas is of a great significance for meeting the requirements for specific products: H_2/CO = 2:1 for methanol and H_2/CO = 1:1 for dimethyl ether for example. The conventional production approach of syngas is based on reforming non-renewable fossil fuels (e.g., coal, petroleum coke, and natural gas)[3], which increases the consumption of fossil fuel and aggravates the energy crisis. Synthesizing syngas with a controlled H_2/CO ratio by reduction of CO_2 not only contributes to the solution of the energy crisis, but at the same time reduces the amount of greenhouse gases (CO_2).

CO_2 reduction to CO and hydrogen evolution reactions (HER) per se are two independent major and important fields. Electrochemical (EC) and photoelectrochemical (PEC) methods integrating CO_2 reduction reaction and HER are key components of prospective technologies for renewable syngas[4]. Different types of semiconductors have been combined with an efficient catalyst for CO_2 reduction to produce syngas by the PEC approach[5–8]. Cu-ZnO/GaN/n+−p Si was recently reported as a highly efficient PEC catalyst to produce syngas with a tunable H_2/CO ratio (between 1:2 and 4:1)[5]. Metal or metal-based composites, including Ag[9], Cu[10], Ru(II) polypyridyl complex[11], Ag/C_3N_4[12], and Re-functionalized graphene oxide[13], have been investigated for EC reduction of CO_2 and H^+/H_2O to syngas. The different methods used to tune the ratio of H_2/CO include altering the CO_2 flow rate[14] and pressure[15], the reaction temperature[16], and the applied potential[9]. Different crystalline sites of Au catalyze different reaction channels (edge sites initiate CO generation and corner sites H_2 generation)[17, 18]. A novel pulsed-bias technique using Cu as the catalyst was recently applied to tune the H_2/CO ratio in syngas between ~32:1 and 9:16 by using different pulse times for the same working potential. The selectivity is however limited and CH_4 and C_2H_4 by-products affect the purity of syngas[10]. Using Ag/C_3N_4[12], the H_2/CO ratio in the produced syngas can be tuned from 100:1 to 2:1 by controlling the applied potential and the Ag loading on graphitic carbon nitride but the total current density is lower than 1 mA/cm² at −0.6 V. The previous EC attempts to synthesize renewable syngas are still characterized by an unsatisfactory performance including some of the following disadvantages: a high onset overpotential necessary to initiate the CO_2 reduction reaction, a low CO + H_2 generation current density, a small selectivity of CO production, and a poor stability of the generation current density and the Faradaic efficiency (FE) of H_2 and CO.

We hereby propose a design concept of a cheap composite EC catalyst for a tunable, stable, selective, and efficient production of syngas, made of three components: a HER catalyst, a CO_2 reduction catalyst toward CO, and a catalyst which stabilizes the active hydrogen (H•) necessary to trigger both HER and the CO_2 reduction reactions. For HER, we choose several known catalysts (Co_3O_4, Pt, MoS_2, and Au). For CO_2 reduction, we apply graphitic carbon nitride (C_3N_4) since carbon-bonded nitrogen groups including pyridinic N, pyrrolic N, and graphitic N have recently been proposed as active sites for CO_2 reduction to CO[19–21]. C_3N_4 has a porous structure and is shown as a good substrate for dispersion of catalytic nanoparticles[22–25]. The selected catalyst for stabilization of active hydrogen (H•) are carbon dots (CDots)[26, 27], which possess significant adsorption capabilities for H^+[28, 29] and CO_2[30] and exhibit excellent ability of electron transfer[31, 32] necessary for H• generation ($H^+ + e^- \rightarrow$ H•). CDots also improve the conductivity of C_3N_4.
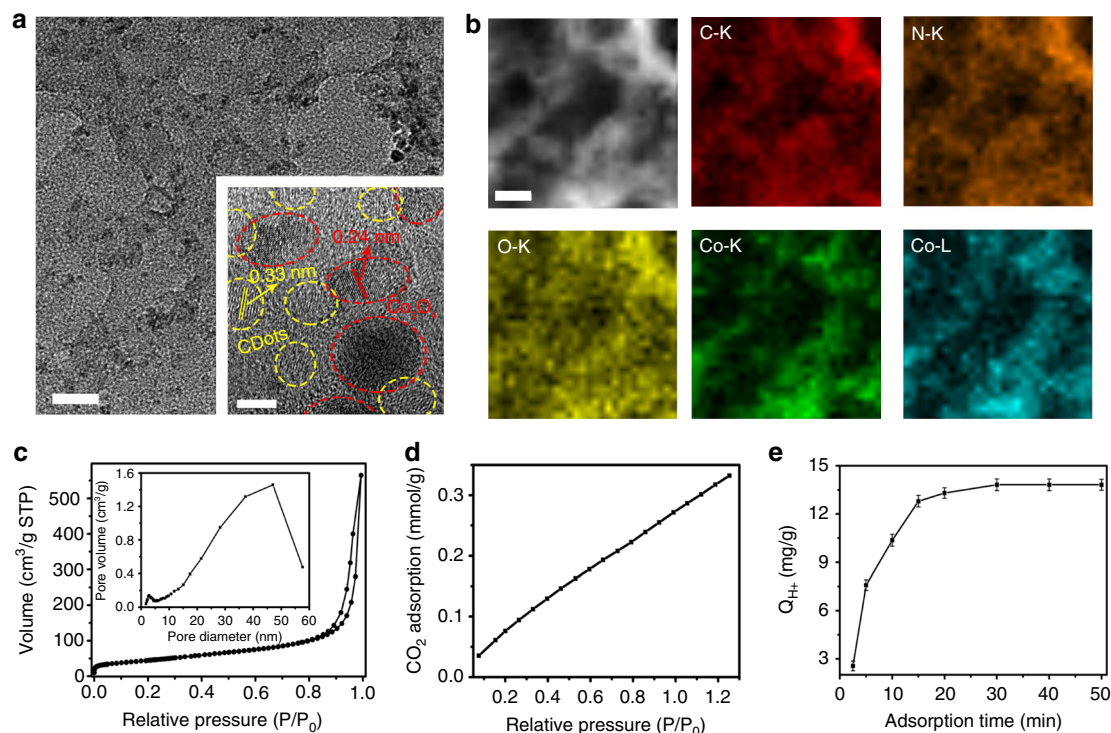

Fig. 1 Characterization of the Co_3O_4-CDots-C_3N_4. **a** TEM image of a grain of the Co_3O_4-CDots-C_3N_4 and a HRTEM image of Co_3O_4-CDots-C_3N_4 (inset), scale bar 20 nm and 5 nm (inset). **b** STEM micrograph and the corresponding elemental mapping of C-K, N-K, O-K, Co-K, and Co-L for the Co_3O_4-CDots-C_3N_4, scale bar 50 nm. **c** N_2 adsorption–desorption isotherm and the corresponding pore-size distribution of Co_3O_4-CDots-C_3N_4 (inset). **d** CO_2 adsorption isotherm of Co_3O_4-CDots-C_3N_4. **e** The time-course adsorption of H^+ by the Co_3O_4-CDots-C_3N_4. The adsorption is 13.8 mg/g. Experiments were performed in triplicates and results are shown as mean ± standard deviation
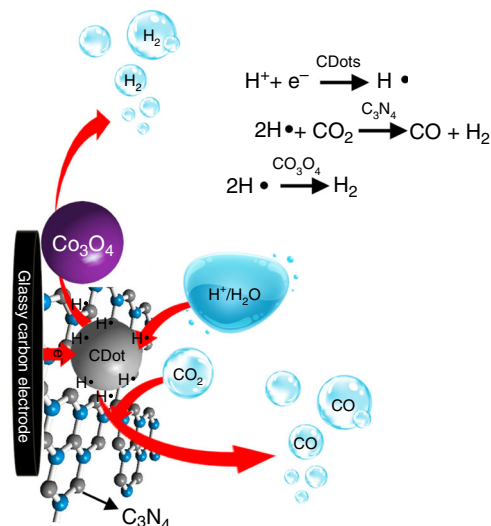
Fig. 2 Schematic diagram of the reaction mechanism induced by Co_3O_4-CDots-C_3N_4. CDots are the generation site of H•, Co_3O_4 the generation site of H_2, and C_3N_4 the generation site of CO

Here we found that the Co_3O_4-CDots-C_3N_4 is the best EC catalyst for syngas production studied within the present work. We thus first describe the structural characterization of this catalyst. We then present the design concept of the three-component catalyst for syngas production and detail its working mechanisms. We follow by showing that this concept is valid and that Co_3O_4-CDots-C_3N_4 is indeed an efficient, tunable, stable, selective, and cheap EC catalyst for syngas production. It initiates CO_2 reduction to CO in aqueous solutions at a low overpotential (0.17 V vs. reversible hydrogen electrode (RHE)) and the total current density of H_2 and CO generation may reach up to 15 mA/cm^2 at a potential of −1.0 V vs. RHE. The H_2/CO ratio of syngas generated by Co_3O_4-CDots-C_3N_4 is tunable from 0.07:1 to 4:1 by controlling the applied potential. Dedicated experiments highlight the different mechanisms by which syngas production applying Co_3O_4-CDots-C_3N_4 is controlled and manipulated. Finally, the generality of the catalyst design concept applying Pt, MoS_2, and Au as the HER catalyst is demonstrated. The significance of this work is thus twofold. First, it presents Co_3O_4-CDots-C_3N_4 as an efficient, cheap, tunable, and stable catalyst for syngas production on one hand. Second, it provides an avenue to design catalysts for controlled and tuned production of syngas in particular and other chemicals of interest to the chemical industry in general.

Results

Characterization of Co_3O_4-CDots-C_3N_4. Transmission electron microscopy (TEM) image (Fig. 1a) reveals that the Co_3O_4-CDots-C_3N_4 consist of nm-sized Co_3O_4 nanoparticles (NPs) and CDots dispersed on the C_3N_4 matrix. The two different types of nanocrystals shown in the inset of Fig. 1a are identified as Co_3O_4 NPs with a d-spacing of 0.24 nm consistent with Co_3O_4 (311)[33] and CDots with an interplanar spacing of 0.33 nm (see Supplementary Fig. 1)[34]. Figure 1b displays a scanning transmission electron microscopy (STEM) micrograph and its corresponding chemical maps of C-K, N-K, O-K, Co-K, and Co-L for the Co_3O_4-CDots-C_3N_4. Co-K, Co-L, and O-K cover the entire C_3N_4 area monitored, indicating that Co_3O_4 NPs are evenly distributed on the C_3N_4 sheet. X-ray diffraction (XRD) shows (Supplementary Fig. 2) the typical diffraction lines of Co_3O_4 and C_3N_4. Besides the average size of Co_3O_4 NPs derived from the XRD spectrum of the Co_3O_4-CDots-C_3N_4 using the Debye–Scherrer equation (Supplementary Table 1), is about 10 nm, which is consistent with the

size of Co_3O_4 NPs in the TEM image. Energy dispersive X-ray absorption (EDX) analysis of the Co_3O_4-CDots-C_3N_4 (Supplementary Fig. 3) reveals an elemental atom composition of C (46.65 at. %), N (48.74 at. %), O (3.01 at. %), and Co (1.60 at. %). X-ray photoelectron spectroscopy (XPS) of the composite (Supplementary Fig. 4) shows C 1s, N 1s, O 1s, and Co 2p peaks with a similar elemental composition to that deduced by EDX (C (39.9 at. %), N (52.5 at. %), O (5.8 at. %), and Co (1.8 at. %)) (Supplementary Table 2). The Co $2p_{3/2}$ peak was fitted (Supplementary Fig. 4e) by using two synthetic peaks positioned at binding energy (BE) = 780.0 and 781.3 eV (Co^{3+} and Co^{2+}, respectively) and the Co $2p_{1/2}$ peak was fitted (Supplementary Fig. 4e) by using two synthetic peaks positioned at BE = 795.0 and 797.3 eV (Co^{3+} and Co^{2+}, respectively). Figure 1c shows type IV N_2 adsorption–desorption isotherms of the Co_3O_4-CDots-C_3N_4 with a H3-type hysteresis loop[35], indicating the formation of a porous structure (the pore-size distribution was derived from the isotherms; for more details, see Supplementary Methods) is presented in Fig. 1c inset; specific surface area ~160 m^2/g). The porous Co_3O_4-CDots-C_3N_4 was found to adsorb a large amount of CO_2 (~0.33 mmol/g at 1.2 atm, Fig. 1d). This strong CO_2 adsorption capability is mainly due to CO_2 molecules adsorbed on the porous C_3N_4 surfaces, which constitute more than 90 wt.% of the composite catalyst (Supplementary Fig. 5a). It is nevertheless enhanced in a synergistic way by the incorporation of CDots (Supplementary Fig. 5b shows that the CO_2 adsorption on Co_3O_4-CDots-C_3N_4 and on CDots-C_3N_4 is about the same, while that on Co_3O_4-C_3N_4 is much lower). The adsorption of H$^+$ (Fig. 1e) is very rapid in the first 15 min, then it becomes slower with contact time, stopping additional absorption after 30 min. The amount of adsorbed H$^+$ (for more details, see Supplementary Methods) on Co_3O_4-CDots-C_3N_4 and CDots-C_3N_4 is about 13.8 mg/g, while the amount of adsorbed H$^+$ is only 5.11 mg/g for the Co_3O_4-C_3N_4 (Supplementary Fig. 6b). The incorporation of CDots thus significantly increases the adsorbed capacity of H$^+$. All these results indicate that the present electrocatalyst has a strong adsorption capacity for both H$^+$ and CO_2, which is significantly important for both processes of CO_2 reduction reaction and HER.

The electrocatalyst design and reaction mechanism. We first present the design concept of the ternary electrocatalyst and highlight its operation mode to produce syngas in a controllable, tunable way. The proposed electrocatalyst consists of three parts: an electrocatalyst for HER (e.g., Co_3O_4), an electrocatalyst for CO_2 reduction to CO (e.g., C_3N_4), and an electrocatalyst which triggers both reaction channels (e.g., CDots by trapping H$^+$ and e$^-$ and generating H•). A schematic diagram of the Co_3O_4-CDots-C_3N_4 ternary electrocatalyst syngas generation is presented in Fig. 2. CDots first trap H$^+$ from the solution and e$^-$ from the glassy carbon electrodes and combine them to form H•. The two other catalyst components compete for these H• species. They may diffuse to C_3N_4 (the CO_2 reduction catalyst due to its different N active sites[19–21]) and reduce CO_2 to CO. Alternatively they may diffuse to Co_3O_4 (the HER catalyst) and produce H_2. We thus suggest that CDots are the generation site of H•, C_3N_4 is the generation site of CO, and Co_3O_4 is the generation site of H_2. Syngas with tunable H_2/CO ratio can be thus achieved by balancing the CO_2 reduction channel and the HER channel. The different catalyst components have additional functions. Introduction of CDots to the composites enhances the adsorption of both CO_2 and H$^+$. Incorporation of CDots in the electrocatalyst improves its conductivity (Supplementary Fig. 7). C_3N_4 serves as the highly porous substrate in which the CDots and Co_3O_4 nanoparticles are incorporated. C_3N_4 thus provides a large surface area which
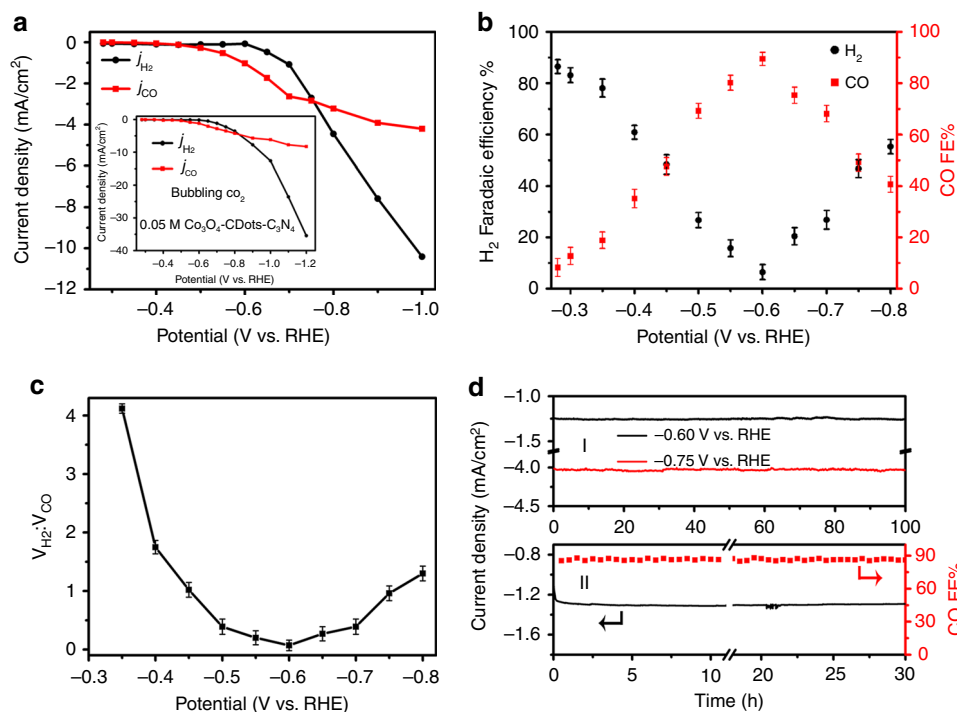
Fig. 3 Electroreduction of CO_2 and H^+/H_2O to syngas with adjustable H_2/CO ratio. **a** The current density for HER (j_{H2}, black trace) and for CO_2 reduction, (j_{CO}, red trace) vs. the applied potential, catalyzed by Co_3O_4-CDots-C_3N_4 in CO_2-saturated 0.5 M $KHCO_3$ electrolyte. The inset shows the same experiment conducted with bubbling of CO_2 to the solution to overcome CO_2 consumption during the experiment. **b** The FEs of the reduction of CO_2 to CO (red points) and H^+ to H_2 (black points) catalyzed by Co_3O_4-CDots-C_3N_4 vs. the applied potential. Experiments were performed in triplicates and results are shown as mean ± standard deviation. **c** The volume ratio between H_2 and CO vs. the applied potential. The H_2/CO volume ratio is about 1:1 at the potential of −0.45 V or −0.75 V vs. RHE. **d** The stability of the performance of Co_3O_4-CDots-C_3N_4 for producing syngas: operated at potentiostatic potential of −0.6 and −0.75 V for 100 h (**dI**); operated at potentiostatic potential of −0.6 V for 30 h (**dII**): current density vs. time (left axis) and FEs of CO production vs. time (right axis)

enhances the reaction activity and also guarantees a proximity between the different generation sites (CDots for H• generation, C_3N_4 for CO generation, and Co_3O_4 for H_2 generation). This proximity is essential for an efficient reaction. Experimental evidence substantiating this proposed mechanism will be given in the following sections.

The electrocatalytic performance of Co_3O_4-CDots-C_3N_4. We now show that the suggested design concept of the Co_3O_4-CDots-C_3N_4 indeed provides a tunable and stable production of syngas. The electrocatalytic performance of Co_3O_4-CDots-C_3N_4 for syngas production was tested in an airtight three electrodes electrochemical H-type cell. The gaseous reduction products monitored by a gas chromatography (GC) system were CO and H_2 while no other reduction liquid products were found by H^1 NMR. Figure 3a shows the current densities of CO (j_{CO}, red trace) and H_2 (j_{H2}, black trace) vs. different potentials acquired in a CO_2-saturated 0.5 M $KHCO_3$ (pH = 7.2) solution. The curves indicate a significant generation of both CO and H_2 but the j_{CO}/j_{H2} ratio varies with the potential applied. The j_{CO} curve shows that the CO_2 electrocatalytic reduction starts at an initial potential of −0.28 V vs. RHE (all potentials reported throughout this paper are with respect to this reference). This operating voltage corresponds to a low overpotential of 0.17 V (the equilibrium potential of CO_2/CO is at −0.11 V). Up to −0.45 V, both j_{CO} and j_{H2} are very small and above −0.45 V both currents increase. Between −0.45 and −0.75 V, j_{CO} is larger than j_{H2}, indicating that the CO_2 reduction reaction predominates. For potentials larger than −0.75 V, the HER channel becomes more significant than the CO_2 reduction reaction. The increase of j_{H2} with potential is about

constant (the j_{H2} curve is a straight line). In contrast, the slope of the j_{CO} curve decreases with the potential applied. We attribute this behavior to the consumption of CO_2 at high CO generation rates due to its low solubility or slow mass transfer. Indeed (inset of Fig. 3a), bubbling CO_2 into the electrolyte increases j_{CO} but the increase rate of j_{CO} with potential is still lower than that of j_{H2}. Figure 3b shows the FEs of CO and H_2 generation vs. the applied cathodic potentials. The FE of CO generation increases with the applied potential and reaches a maximum of 89% at −0.6 V. For higher potential, it decreases to ~40% with increasing potential to −0.8 V, most probably due to the limited mass transport of CO_2 in the electrolyte. In contrast, the FE of H_2 generation is about 86% for a low applied potential, decreases with potential to about 5% at −0.6 V and then rises again reaching 55% at −0.8 V. The total FE of CO and H_2 combined reaches up to 95%. Consequently, syngas with different H_2/CO ratios can be obtained by altering the applied potential as shown in Fig. 3c. The volume ratio between H_2 and CO can be tuned from 4:1 to 0.07:1 and syngas with $H_2/CO = 1:1$ can directly be generated at the potentials of −0.45 V (total current density is 0.25 mA/cm^2) and −0.75 V (total current density is 5.78 mA/cm^2). Note that the catalyst mass activity for syngas generation reaches a high value of 10 A/g$_{catalyst}$ at a potential of −0.6 V. The stability of the Co_3O_4-CDots-C_3N_4 catalyst for electrocatalytic CO_2 reduction and HER (Fig. 3d) was studied as well. A negligible decay in current density was observed when operating the system for 100 h at the applied potential of both −0.6 V (Fig. 3dI, black trace, CO_2 reduction reaction predominates) and −0.75 V (Fig. 3dI, red trace, HER and CO_2 reduction are equal). It reveals that the Co_3O_4-CDots-C_3N_4 maintains high electrocatalytic stability during the 100-h test. An additional experiment validated the stability of
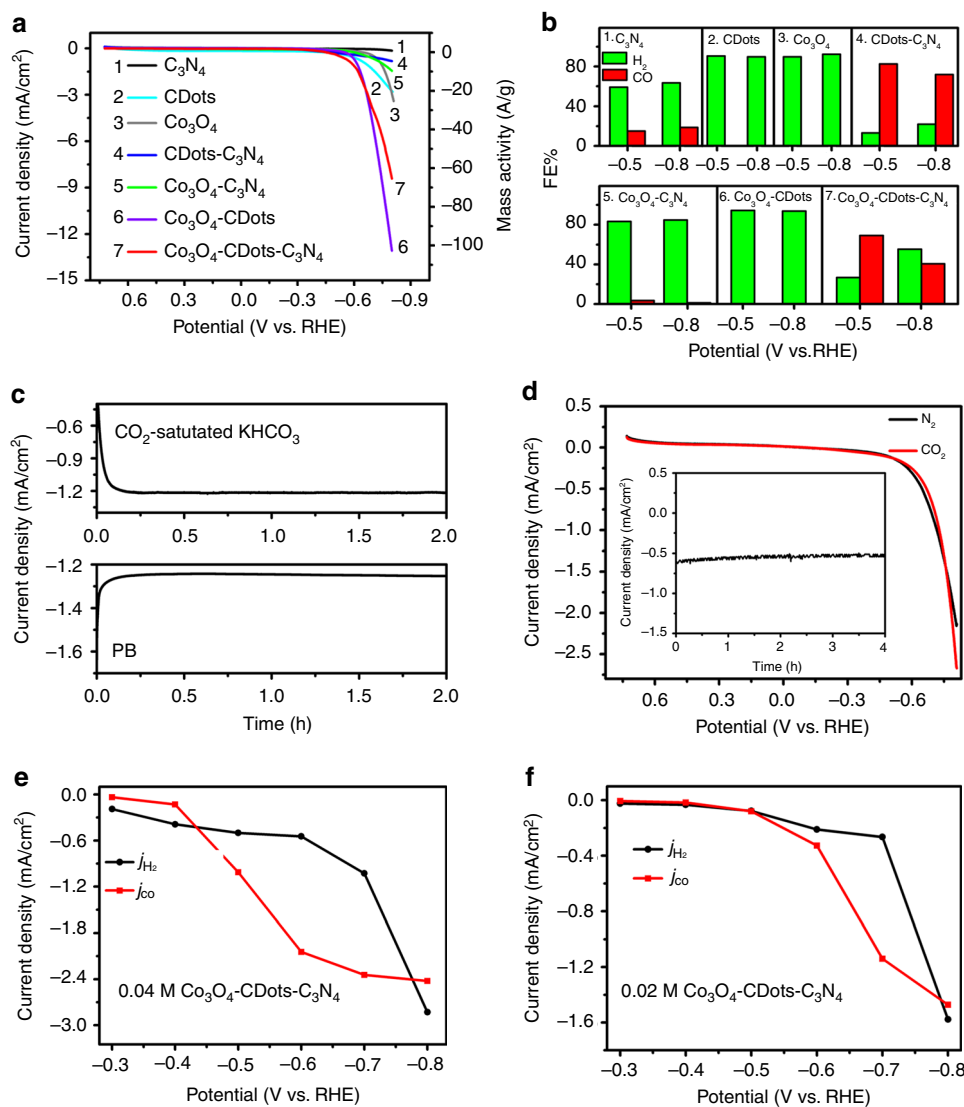
Fig. 4 Electrochemical experiments providing insight into the electrochemical processes. **a** The linear sweep voltammetry curves (LSVs) for C_3N_4 (black trace, curve 1), CDots (cyan trace, curve 2), Co_3O_4 (gray trace, curve 3), CDots-C_3N_4 (blue trace, curve 4), Co_3O_4-C_3N_4 (green trace, curve 5), Co_3O_4-CDots (purple trace, curve 6), and Co_3O_4-CDots-C_3N_4 (red trace, curve 7) in CO_2-saturated 0.5 M $KHCO_3$ electrolyte, 10 mV/s. Current density on left y axis and mass activity on right y axis. The comparison of the curves allows determination of the role of the different catalyst components in the electrochemical reactions. **b** The FEs of the reaction products at −0.5 and −0.8 V, using C_3N_4, CDots, Co_3O_4, CDots-C_3N_4, Co_3O_4-C_3N_4, Co_3O_4-CDots, and Co_3O_4-CDots-C_3N_4, respectively, as catalysts. Note that only the C_3N_4 and CDots-C_3N_4 composites produce significant amounts of CO. **c** Total current density vs. time curves of CO_2 reduction to CO and HER at the potential of −0.6 V in CO_2-saturated $KHCO_3$ solution (0.5 M, pH = 7.2) and phosphate buffer (PB) solution (pH = 7.2), respectively. **d** LSVs for the Co_3O_4-CDots-C_3N_4 in N_2- (black trace) and CO_2-saturated (red trace) MeCN containing 0.5 M [BMIM]PF_6, 10 mV/s. The inset shows the total current density vs. time curves of CO_2 reduction at the potential of −0.6 V in CO_2-saturated MeCN containing 0.5 M [BMIM]PF_6. The current in the inset is much smaller than in **c** and no reaction products are detected indicating that H^+ is essential for both HER and CO_2 reduction to CO. **e** Current density for HER (j_{H_2}, black trace) and current density for CO_2 reduction, (j_{CO}, red trace) vs. the applied potential, catalyzed by 0.04 M Co_3O_4-CDots-C_3N_4 in a CO_2-saturated 0.5 M $KHCO_3$ electrolyte. **f** Current density for HER (j_{H_2}, black trace) and current density for CO_2 reduction, (j_{CO}, red trace) vs. the applied potential, catalyzed by 0.02 M Co_3O_4-CDots-C_3N_4 in CO_2-saturated 0.5 M $KHCO_3$ electrolyte; note that the reduction of the amount of the HER catalyst component shifts the balance of gas generation toward enhanced CO generation

both the current density and the FE for 30 h (it is very likely that the FE is stable for 100 h as well).

Investigation of the catalytic mechanisms. A series of controlled experiments were carried out to validate and further understand the catalytic mechanism operating with the Co_3O_4-CDots-C_3N_4 proposed in a previous section (Fig. 2). Issues investigated included: the generation sites of H•, CO, and H_2; the role of H^+; the roles of CDots, C_3N_4, and Co_3O_4; the role of the proximity between the CDots, C_3N_4, and Co_3O_4; ways in which the relative

significance of the different reaction channels and the resulting CO/H_2 volume ratio can be manipulated; other HER-CDots-C_3N_4 systems with different HER materials. We first studied the linear sweep voltammetry (LSV) curves of different combinations of the three components comprising the ternary Co_3O_4-CDots-C_3N_4. The comparison of the different LSV curves (Fig. 4a) and the complementary study of the CO and H_2 composition generated during the electrocatalytic processes catalyzed by the different components (Fig. 4b) enabled a clear determination of both the generation sites of the CO and H_2 and the role of the three basic components used. We first discuss the LSVs showing the apparent

current density (current density per geometrical area), which is also equivalent to the mass activity of the catalysts (current per gram catalyst) as shown in Fig. 4a. Further on, we also give the corresponding turn on frequencies (TOFs) and the real current densities derived from the real surface areas of the components of the different combinations of catalysts in Fig. 4a. LSVs of C_3N_4 (Fig. 4a, curve 1, black trace, morphology of C_3N_4 is shown in Supplementary Fig. 8a), CDots (Fig. 4a, curve 2, cyan trace, morphology of CDots is shown in Supplementary Fig. 1), Co_3O_4 (curve 3, gray trace, morphology of Co_3O_4 is shown in Supplementary Fig. 8b), CDots-C_3N_4 (curve 4, blue trace, morphology of CDots-C_3N_4 is shown in Supplementary Fig. 8c), Co_3O_4-C_3N_4 (curve 5, green trace, morphology of Co_3O_4-C_3N_4 is shown in Supplementary Fig. 8d), Co_3O_4-CDots (curve 6, purple trace, morphology of Co_3O_4-CDots is shown in Supplementary Fig. 8e), and Co_3O_4-CDots-C_3N_4 (curve 7, red trace) were performed using a CO_2-saturated 0.5 M $KHCO_3$ (pH = 7.2) solution (Fig. 4a). The LSVs of C_3N_4 (curve 1, black trace), CDots (curve 2, cyan trace), Co_3O_4 (curve 3, gray trace), CDots-C_3N_4 (curve 4, blue trace), and Co_3O_4-C_3N_4 (curve 5, green trace) show poor electrocatalytic performances evident by their low current densities and high onset potentials (Fig. 4a). Only the Co_3O_4-CDots (curve 6) and the Co_3O_4-CDots-C_3N_4 (curve 7) exhibit high current densities and low onset potentials (Fig. 4a). CDots generate H_2 only, but not CO (Fig. 4b). We explain it by their trapping and stabilizing H•, which may generate a small amount of H_2 even in the absence of a HER catalyst. The LSV of Co_3O_4 (curve 3, gray trace) shows a relatively small activity producing only H_2 (Fig. 4b). In comparison, Co_3O_4-CDots (curve 6, purple trace) produces a much larger amount of H_2 compared to pure CDots or pure Co_3O_4. We attribute it to the effect of the CDots, which greatly enhance the electrocatalytic performance of Co_3O_4 by providing H•, which is necessary for generation of H_2. We thus conclude that Co_3O_4 is the H_2 generation site while CDots are the generation site of H• and both are needed for a large generation rate of H_2. Now, we prove that the generation site of CO is C_3N_4. Figures 3a, b and 4a, b indicate that significant amounts of CO are generated by either the CDots-C_3N_4 or the Co_3O_4-CDots-C_3N_4. Co_3O_4 was shown to generate H_2 only, which leaves CDots-C_3N_4 as the producer of CO. CDots per se produce only H_2 as previously discussed. They however are essential for CO generation by CDots-C_3N_4 since they significantly enhance the CO_2 adsorption, adsorb H^+, and stabilize H•. C_3N_4 per se catalyzes only a very small (negligible) current (Fig. 4a, curve 1) so that the very little amount of gas produced by pure C_3N_4 (Fig. 4b) contains more H_2 than CO. The supply of H• by the CDots is necessary to promote the generation of CO in C_3N_4. Figure 4a shows that each catalyst component adds to the activity by enhancing one of the three reactions (H• generation, H_2 generation, and CO generation) but the complete three components composite Co_3O_4-CDots-C_3N_4 is necessary for intense generation of syngas. We further studied the effect of the type of mixing of the different catalyst components on the catalytic activity. The LSVs of physical mixtures of catalysts (Co_3O_4 + C_3N_4, CDots + C_3N_4, and Co_3O_4 + CDots + C_3N_4) were compared to those of composites of the same components chemically blended (Co_3O_4-C_3N_4, CDots-C_3N_4, and Co_3O_4-CDots-C_3N_4). The chemically prepared composites had much larger activities (current densities) than their corresponding physical mixtures (Supplementary Fig. 9). We attribute the large activity of the chemically prepared composites to the close proximity between the different catalysts (active sites) in the composite materials. In contrast, physical mixing does not provide such a proximity so that the large distance between the active sites hinders the activity of the physically mixed catalysts.

The comparison between the LSVs of the different catalyst components and their composites (Fig. 4a) should be done

carefully. The catalyst areal density was kept the same (0.127 mg/cm^2) for all (3 mm in diameter) electrodes. Since the composition of the Co_3O_4-CDots-C_3N_4 was 6 wt% Co_3O_4, 1 wt% CDots, and 93 wt% C_3N_4, it follows that the amount of CDots or Co_3O_4 in the CDots, Co_3O_4, or Co_3O_4-CDots electrodes was much larger than in the C_3N_4 containing composite electrodes. This means that the reaction activity per catalyst mass of curves 2, 3, and 6 is very low compared to that of the Co_3O_4-CDots-C_3N_4 electrode (Fig. 4a, curve 7). Since we deal with three different catalysts with different functions, we should calculate the mass activity (current per gram catalyst) for each component separately. This was done in Supplementary Fig. 10. The reaction activity per mass of a single catalyst component (Co_3O_4 or CDots) of Co_3O_4-CDots (Fig. 4a, curve 6), e.g., is actually lower by more than an order of magnitude than the activity per mass of a single catalyst component of that of the Co_3O_4-CDots-C_3N_4 catalyst (Fig. 4a, curve 7) though curve 6 appears to indicate (Fig. 4a) a larger activity than curve 7 (compare Fig. 4a to Supplementary Fig. 10). Supplementary Fig. 10 clearly shows that starting from a single catalyst component, the addition of each of the two other components increases the activity of syngas production, i.e., all components are necessary for an optimized syngas generation. Similarly, we calculate the turn on frequencies (TOFs) of the catalysts compositions of Fig. 4a. TOF = (number of reacted electrons per time/number of catalyst active sites). We approximate the number of active sites by the number of catalyst atoms. Since we have three different catalyst components with three different functions, we calculate the TOFs per each catalyst component (CDots, Co_3O_4, and C_3N_4). Supplementary Fig. 11 shows (similar to Supplementary Fig. 10) that the addition of each single component increases the syngas production activity and all components are necessary for the optimal performance. We further measure the BET and the electrochemical real surface areas of the catalyst components of each combination shown in curves 1–7 (Supplementary Tables 3–4). We use the electrochemical surface areas (ECSAs) to calculate the real current densities related to the specific catalyst components that constitute the seven combinations shown in curves 1–7. Supplementary Fig. 12 shows that similar to the mass activities and the TOFs curves, the real current densities of one component increase with the addition of a second component and are the largest when all three catalyst components combine to a three-component catalyst composite. Figure 3 shows that the ternary concept design indeed yields an optimal performance of its different components balancing between CO_2 reduction and HER. This explains the high value of 10 A/$g_{catalyst}$ obtained at −0.6 V. The CO_2 and H^+ adsorption measurements (Supplementary Figs. 5 and 6) of the individual different catalyst components (CDots, Co_3O_4, and C_3N_4) and their composites (CDots-C_3N_4, Co_3O_4-C_3N_4, CDots-Co_3O_4, and CO_3O_4-CDots-C_3N_4) reveal another effect which improves the ternary composite catalyst performance. The synergism of the three components acting simultaneously enhances the adsorption of the ternary composite by a factor of 2–3 with respect to the adsorption of the individual components. Real surface area measurements (BET and electrochemical) of the catalyst compositions (Supplementary Table 3) indicate that the inclusion of the C_3N_4 component results in a high surface area (($S_{real}/S_{geometrical}$) = 200 for BET and 30 for electrochemical) while it is lower by an order of magnitude for the nanoparticle catalysts (CDots, Co_3O_4, or CDots-Co_3O_4). The dispersion of the catalysts nanoparticles on the C_3N_4 surface seems to explain the synergistic adsorption behavior.

To study the role of H^+ in syngas generation, we investigated the electrocatalytic performance of Co_3O_4-CDots-C_3N_4 in aqueous solutions with the same pH value (HER in phosphate buffer solution, pH = 7.2; syngas reaction in CO_2-saturated 0.5 M
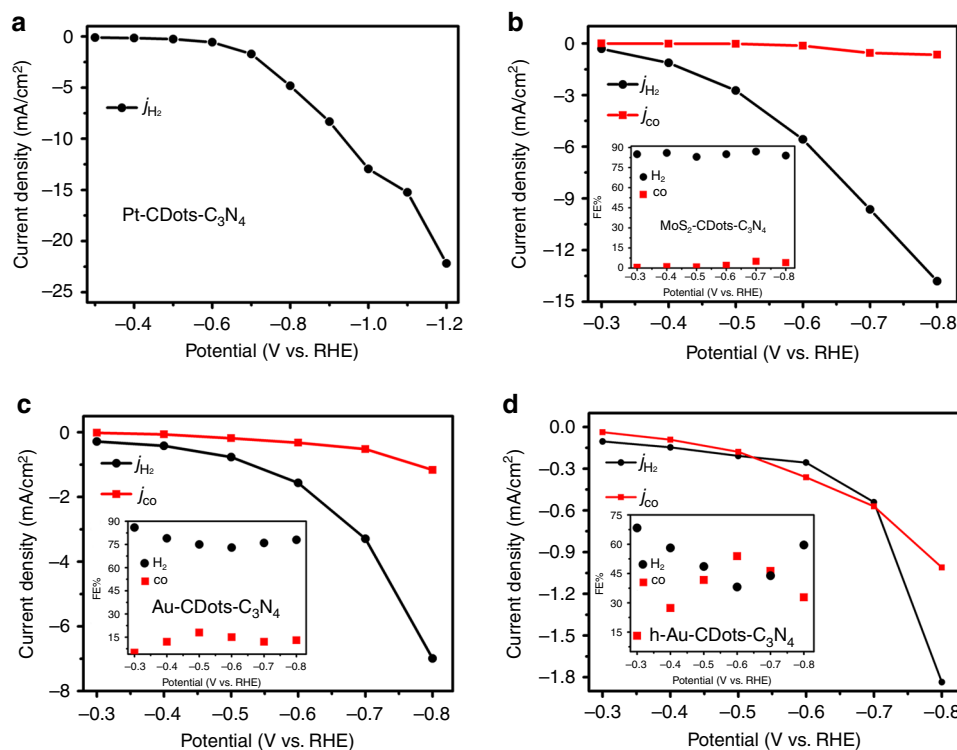
Fig. 5 Catalytic activity of composite catalysts with different HER catalysts. **a** Current density for HER (j_{H2}, black trace) vs. the applied potential, catalyzed by Pt-CDots-C_3N_4 in CO_2-saturated 0.5 M KHCO$_3$ electrolyte. **b** Current density for HER (j_{H2}, black trace) and current density for CO_2 reduction to CO, (j_{co}, red trace) and FEs of H_2 and CO (inset) vs. the applied potential, catalyzed by MoS$_2$-CDots-C_3N_4 in CO_2-saturated 0.5 M KHCO$_3$ electrolyte. **c** Current density for HER (j_{H2}, black trace) and current density for CO_2 reduction, (j_{co}, red trace) and FEs of H_2 and CO (inset) vs. the applied potential, catalyzed by Au-CDots-C_3N_4 in CO_2-saturated 0.5 M KHCO$_3$ electrolyte. **d** Current density for HER (j_{H2}, black trace) and current density for CO_2 reduction, (j_{co}, red trace) and FEs of H_2 and CO (inset) vs. the applied potential, catalyzed by Au-CDots-C_3N_4 in CO_2-saturated 0.5 M KHCO$_3$ electrolyte. The amount of Au in **d** is half of that in **c** (marked as h-Au-CDots-C_3N_4) leading to an increase of the CO/H_2 ratio in **d** with respect to that in **c**

KHCO$_3$ solution, pH = 7.2) and in an ionic liquid (without H^+). The current density–time curves of pure HER and syngas reactions at the potential of −0.6 V (at −0.6 V the syngas reaction produces ~90% CO) are shown in Fig. 4c. A stable current density (~−1.21 mA/cm^2) for syngas is observed at −0.6 V while −1.25 mA/cm^2 for HER is reached at the same potential. Then, ionic liquid was used as the electrolyte solution to eliminate H^+. The electrocatalytic performance of Co$_3$O$_4$-CDots-C_3N_4 was tested at the potential of −0.6 V in a CO_2-saturated MeCN solution containing 0.5 M [BMIM]PF$_6$. The current density is only about 0.61 mA/cm^2 in a CO_2-saturated ionic liquid (Fig. 4d), which is much lower than that obtained for CO_2 reduction in CO_2-saturated KHCO$_3$ solution (−1.21 mA/cm^2). Notably, no gaseous products of CO reduction could be detected suggesting that H^+ plays an important role for CO_2 reduction to CO in the present Co$_3$O$_4$-CDots-C_3N_4 catalyst system.

It was shown that the H_2/CO volume ratio obtained using the Co$_3$O$_4$-CDots-C_3N_4 catalyst system is determined by the balance between the HER channel and the CO_2 reduction channel to CO. This ratio was tuned by modifying the potential (Fig. 3). Another plausible tuning method is the decrease of the amount of the HER catalyst component (Co$_3$O$_4$) thus reducing the HER activity and increasing the CO_2 reduction activity. We therefore measured the electrocatalytic activities of Co$_3$O$_4$-CDots-C_3N_4 produced using lower amounts of Co (0.04 and 0.02 M Co$_3$O$_4$ loadings with respect to the standard one of the present work (0.05 M)). Figures 3a and 4e, f show the j_{H2} and j_{CO} obtained at different applied potentials for 0.05, 0.04, and 0.02 M Co$_3$O$_4$-CDots-C_3N_4, respectively. It is obvious that the CO/H_2 ratio was strongly affected by the change of the Co$_3$O$_4$ HER catalyst amount.

Finally, the design concept of the HER-CDots-C_3N_4 ternary catalyst was applied for three additional HER active electrocatalysts: Pt, MoS$_2$, and Au to form Pt-CDots-C_3N_4, MoS$_2$-CDots-C_3N_4, and Au-CDots-C_3N_4. The structural characterization of these catalysts is given in Supplementary Fig. 13. The electrocatalytic activity of these three ternary composite catalysts for producing syngas were tested under the same conditions as for Co$_3$O$_4$-CDots-C_3N_4. Applying the Pt-CDots-C_3N_4 electrocatalyst (Fig. 5a), only hydrogen was detected in the gas phase and no reduction products from CO_2 reduction were observed. Pt is considered as the most efficient electrocatalyst to facilitate HER[36]. The application of Pt-CDots-C_3N_4 as a catalyst shifts the balance between HER and CO_2 reduction toward H_2 generation, increases the intensity of the efficient HER channel and completely suppresses the CO_2 reduction to CO. The MoS$_2$-CDots-C_3N_4 electrocatalyst is still sufficiently HER active to produce close to 90% j_{H2}, but a small amount of j_{CO} (a few percent of the total current) is nevertheless observed. The FEs of CO are no more than 10% for the MoS$_2$-CDots-C_3N_4 (inset of Fig. 5b). The Au-CDots-C_3N_4 electrocatalyst (Fig. 5c) still exhibits a higher HER activity than the CO_2 reduction activity, but the amount of CO is much larger than for the MoS$_2$-CDots-C_3N_4 catalyst (the FE of CO production reaches 25%, inset of Fig. 5c). It can be thus concluded that the concept of the ternary HER-CDots-C_3N_4 is general and valid for HER catalysts different than Co$_3$O$_4$. Achievement of a relatively high amount of CO/H_2 however requires the application of a HER catalyst with only a medium activity pushing the balance between HER and CO_2 reduction toward CO_2 reduction. The smaller the HER activity, the larger relative amount of CO is obtainable. This conclusion

was directly checked by reducing the amount of Au in the ternary Au-CDots-C_3N_4 electrocatalyst. The electrochemical tests (Fig. 5d) show that decreasing the amount of Au by a factor of two enabled the generation of syngas with a CO to H_2 volume ratio larger than one. A striking property of the h-Au-CDots-C_3N_4 catalyst is its extremely high mass activity for producing syngas, i.e., >700 A/g_{Au} for CO production and >700 A/g_{Au} H_2 production (~1500 A/g_{Au} for the total current) at −0.7 V for the catalyst shown in Fig. 5d. This activity is two orders of magnitude larger than previously reported for efficient Au electrodes for CO production[17, 18]. This high mass activity allows a reduction of the electrode cost when precious catalysts (e.g., Au) are applied.

Discussion

The design concept of the HER-CDots-C_3N_4 EC catalyst for syngas generation was introduced and its electrocatalytic performance for syngas production in aqueous solutions was studied, applying Co_3O_4, MoS_2, Au, and Pt as the HER catalyst component. The Co_3O_4-CDots-C_3N_4 electrocatalyst was found the most efficient for syngas production among the composite combinations investigated. The Co_3O_4-CDots-C_3N_4 is capable of controlling the balance between the HER channel and CO_2 reduction channel. The Co_3O_4-CDots-C_3N_4 initiates the reaction of CO_2 reduction to CO in aqueous solutions at a low overpotential (0.17 V) while the total current density reaches up to 15 mA/cm² at a potential of −1.0 V. The mass activity of the Co_3O_4-CDots-C_3N_4 is ~10 A/$g_{catalyst}$ at −0.6 V when the total mass of the catalyst is considered and 1–2 orders of magnitude larger when the mass of the HER catalyst is considered (which is ~0.5–5% of that of the total catalyst weight). The Co_3O_4-CDots-C_3N_4 induces high FEs (95%) and is characterized by a stable production of syngas (over 100 h). Notably, the H_2/CO ratio of syngas produced applying Co_3O_4-CDots-C_3N_4 is tunable from 0.07:1 to 4:1 by controlling the applied potential. The H_2/CO may be also tuned by varying the amount of Co_3O_4 in the Co_3O_4-CDots-C_3N_4.

Dedicated experiments validated the catalyst design concept and provided additional insight to the syngas generation processes. C_3N_4 and Co_3O_4 are the activity sites for CO_2 reduction reaction and HER, respectively. CDots are the generation site of H• needed to trigger both the reduction of CO_2 to CO and the HER. The three-component catalyst concept is a general one and may be applied to a host of other materials. The versatility of the three components composite design may open a powerful pathway for the development of high-performance catalysts for syngas production as well as for other chemicals generation. Such an efficient and cost-effective electrocatalytic system has a high potential to be employed for the large-scaled production of syngas and controlled mixtures of other chemicals from CO_2.

Methods

Instruments. Transmission electron microscopy (TEM), high-resolution transmission electron microscopy (HRTEM), and scanning TEM (STEM) images were obtained using a FEI/Philips Tecnai G2 F20 TWIN transmission electron microscope. The energy dispersive X-ray spectroscopy (EDS) analyses were taken on a FEI-quanta 200 scanning electron microscope with an acceleration voltage of 20 kV . The crystal structure of the resultant products was characterized by X-ray diffraction (XRD) using an X'Pert-ProMPD (Holland) D/max-γAX-ray diffractometer with Cu Kα radiation (λ = 0.154178 nm). X-ray photoelectron spectroscopy (XPS) was obtained by using a KRATOS Axis ultra-DLD X-ray photoelectron spectrometer with a monochromatized Mg Kα X-ray source ($h\nu$ = 1283.3 eV). The electrocatalysis reactions were tested by a Model CHI 660C workstation (CH Instruments, Chenhua, Shanghai, China). The electrochemical impedance spectroscopy (EIS) measurements were obtained applying a CHI 832 electrochemical instrument (CHI Inc., USA).

Materials. $KHCO_3$ (99.7%) and Nafion perfluorinated resin solution (5 wt.%) were purchased from Sigma-Aldrich; hydrogen (99.999%), nitrogen (99.999%), and carbon dioxide (99.999%) were purchased from Airgas; Nafion®212 membrane was

purchased from Dupont; Toray Carbon Paper (TGP-H-60) was purchased from Alfa Aesar; All chemicals were purchased from Sigma-Aldrich unless specifically stated. Milli-Q ultrapure water (Millipore, ≥18 MΩ/cm) was used throughout the work.

Fabrication of electrocatalysts. CDots were synthesized by our previously reported electrochemical etching method[34]. After 30-days reaction, a dark yellow solution containing CDots was formed in the reaction cell. It was then purified and concentrated to form a CDots solution of 3 mg/mL. For C_3N_4 fabrication, 10 g of melamine powder was put into an alumina crucible with a cover and then heated to 550 °C at a rate of 0.5 °C per min in a muffle furnace and maintained at this temperature for 3 h. The yellow powder (C_3N_4) was obtained after cooling down to room temperature. Co_3O_4 NPs was synthesized by hydrothermal method. Twenty mL $Co(NO_3)_2$ (0.01 M) solution was added into an alumina crucible with a cover and then heated to 550 °C at a rate of 0.5 °C per min in a muffle furnace and maintained at this temperature for 3 h. The black powder (Co_3O_4 NPs) was obtained after cooling down to room temperature. For preparation of Co_3O_4-C_3N_4, CDots-C_3N_4 or Co_3O_4-CDots-C_3N_4, 10 g of melamine powder was mixed with 10 mL solution containing 0.05 M $Co(NO_3)_2$, CDots, CDots and 0.05 M $Co(NO_3)_2$, respectively. Then, the mixture was put into an alumina crucible with a cover and heated to 550 °C at a rate of 0.5 °C per min in a muffle furnace and maintained at this temperature for 3 h. For preparation of Co_3O_4-CDots, 10 mL solution containing 0.05 M $Co(NO_3)_2$ and CDots (3 mg/mL) was put into an alumina crucible with a cover and heated to 550 °C at a rate of 0.5 °C per min in a muffle furnace and maintained at this temperature for 3 h.

Synthesis of Pt-CDots-C_3N_4. An aliquot of 0.3 g CDots-C_3N_4 (obtained by heating melamine at 550 °C for 3 h) was added into 10 mL H_2PtCl_6 (2 mM) aqueous solution and stirred for 12 h. After centrifuging, the precipitate was irradiated by UV light for 10 h. The resulting product was collected by centrifugation and dried in a vacuum at 60 °C for 12 h.

Synthesis of MoS_2-CDots-C_3N_4. An aliquot of 0.3 g CDots-C_3N_4 (obtained by heating melamine at 550 °C for 3 h) was added into 15 mL aqueous solution containing Na_2MoO_4 (0.0625 g) and L-cysteine (0.1 g). The mixed solution was stirred 3 min. After that, the mixture was poured into a Teflon-lined stainless steel autoclave, and heated at 180 °C for 24 h. After the autoclave was cooled down to room temperature, the resulting black sediments were collected by centrifugation (10,000 rpm, 10 min) and washed with deionized water and ethanol for several times, and then dried in a vacuum oven at 80 °C for 12 h[37].

Synthesis of Au-CDots-C_3N_4 and h-Au-CDots-C_3N_4. An aliquot of 0.3 g CDots-C_3N_4 (obtained by heating melamine at 550 °C for 3 h) was added into 10 mL $HAuCl_4$ (2 mM or 1 mM) aqueous solution and stirred for 12 h. After centrifuging, the precipitate was irradiated by UV light for 2 h. The resulting product was collected by centrifugation and dried in vacuum at 60 °C for 12 h[38].

Electrocatalysis activity test. Electrocatalysis activity test experiments were performed using a standard three-electrode configuration. A platinum wire was used as an auxiliary electrode and a saturated calomel electrode (SCE) was used as a reference electrode. The working electrode was either a catalyst-modified carbon fiber paper electrode (CFPE for short, 0.7 cm × 0.7 cm), or a catalyst-modified glassy carbon disk electrode (GCE for short, 3.0 mm diameter). For product analysis and constant-potential electrolysis experiment, the CFPE working electrode was a catalyst-modified carbon fiber paper electrode (0.7 cm × 0.7 cm). The preparation of the CFPE working electrode is as follows. An aliquot of 1.3 mg of electrocatalyst was ground with 0.1 mg polyvinylidene fluoride (PVDF) with a few drops of 1-methyl-2-pyrrolidone (MP) added to the produced mixture. The mixture was added into 10 mL 0.5% Nafion solution. After sonication, 1 mL dispersed solution was dropped directly onto the two sides of a 0.7 cm × 0.7 cm carbon fiber paper (the two sides of the carbon paper were modified by the catalyst). The bulk electrolysis was performed in an airtight electrochemical H-type cell with three electrodes. H-type cell consists of two compartments (volume of each part is 115 mL) separated by a Nafion®212 anion exchange membrane with 75 mL 0.5 M $KHCO_3$ electrolyte in each chamber and. Besides, LSV experiments were used with the catalyst-modified GCE as the working electrode. The preparation of the GCE working electrode is as follows. 6 mg electrocatalyst was added into 2 mL 0.5% Nafion solution. After sonication, 3 µL dispersed solution was dropped on GCE. The mass density of catalyst was 0.127 mg/cm². The electrochemical tests of different catalysts combinations were performed with full loading, i.e., the mass of the composite catalyst was 9 µg (Supplementary Table 4). The electrochemical surface area (ECSA) test of single catalyst components were performed using partial loading, i.e., 1% of 9 µg CDots and 6% of 9 µg Co_3O_4 (Supplementary Table 4). For LSVs experiments, initially, polarization curves for the modified electrode were carried out under an inert N_2 (gas) atmosphere. After this, the solution was purged with CO_2 (99.999%) for at least 30 min (CO_2-saturated high purity aqueous 0.5 M $KHCO_3$) and the electrocatalytic CO_2 reduction was measured.

References

1. Klerk, A. Fischer-Tropsch fuels refinery design. *Energy Environ. Sci.* **4**, 1177–1205 (2011).
2. Calderone, V. R. et al. De novo design of nanostructured iron–cobalt Fischer–Tropsch catalysts. *Angew. Chem. Int. Ed.* **52**, 4397–4401 (2013).
3. Goeppert, A. et al. Recycling of carbon dioxide to methanol and derived products–closing the loop. *Chem. Soc. Rev.* **43**, 7995–8048 (2014).
4. Nguyen, V. N. & Blum, L. Syngas and synfuels from H_2O and CO_2: current status. *Chem. Ing. Tech.* **87**, 354–375 (2015).
5. Chu, S. et al. Tunable syngas production from CO_2 and H_2O in an aqueous photoelectrochemical cell. *Angew. Chem. Int. Ed.* **55**, 14262–14266 (2016).
6. Schreier, M. et al. Covalent immobilization of a molecular catalyst on Cu_2O photocathodes for CO_2 reduction. *J. Am. Chem. Soc.* **138**, 1938–1946 (2016).
7. Jang, Y. J. et al. Selective CO production by Au coupled ZnTe/ZnO in the photoelectrochemical CO_2 reduction system. *Energy Environ. Sci.* **8**, 3597–3604 (2015).
8. Jang, Y. J. et al. Unbiased sunlight-driven artificial photosynthesis of carbon monoxide from CO_2 using a ZnTe-based photocathode and a perovskite solar cell in tandem. *ACS Nano* **10**, 6980–6987 (2016).
9. Delacourt, C., Ridgway, P. L., Kerr, J. B. & Newman, J. Design of an electrochemical cell making syngas ($CO+H_2$) from CO_2 and H_2O reduction at room temperature. *J. Electrochem. Soc.* **155**, B42–B49 (2008).
10. Kumar, B. et al. Controlling the product syngas H_2:CO ratio through pulsed-bias electrochemical reduction of CO_2 on copper. *ACS Catal.* **6**, 4739–4745 (2016).
11. Kang, P., Chen, Z., Nayak, A., Zhang, S. & Meyer, T. J. Single catalyst electrocatalytic reduction of CO_2 in water to H_2+CO syngas mixtures with water oxidation to O_2. *Energy Environ. Sci.* **7**, 4007–4012 (2014).
12. Sastre, F. et al. Efficient electrochemical production of syngas from CO_2 and H_2O by using a nanostructured Ag/g-C_3N_4 catalyst. *ChemElectroChem* **3**, 1497–1502 (2016).
13. Zhou, X. et al. Graphene-immobilized fac-Re(bipy)$(CO)_3$Cl for syngas generation from carbon dioxide. *ACS Appl. Mater. Interfaces* **8**, 4192–4198 (2016).
14. Dufek, E. J., Lister, T. E. & McIlwain, M. E. Bench-scale electrochemical system for generation of CO and syn-gas. *J. Appl. Electrochem.* **41**, 623–631 (2011).
15. Dufek, E. J., Lister, T. E., Stone, S. G. & McIlwaina, M. E. Operation of a pressurized system for continuous reduction of CO_2. *J. ElectroChem. Soc.* **159**, 514–517 (2012).
16. Li, Y. H., Li, P., Hua, B. B. & Xia, C. R. A nanostructured ceramic fuel electrode for efficient CO_2/H_2O electrolysis without safe gas. *J. Mater. Chem. A* **4**, 9236–9243 (2016).
17. Zhu, W. et al. Monodisperse Au nanoparticles for selective electrocatalytic reduction of CO_2 to CO. *J. Am. Chem. Soc.* **135**, 16833–16836 (2013).
18. Zhu, W. et al. Active and selective conversion of CO_2 to CO on ultrathin Au nanowires. *J. Am. Chem. Soc.* **136**, 16132–16135 (2014).
19. Sharma, P. P. et al. Nitrogen-doped carbon nanotube arrays for high-efficiency electrochemical reduction of CO_2: on the understanding of defects, defect density, and selectivity. *Angew. Chem.* **127**, 13905–13909 (2015).
20. Wu, J. et al. Incorporation of nitrogen defects for efficient reduction of CO_2 via two-electron pathway on three-dimensional graphene foam. *Nano Lett.* **16**, 466–470 (2015).
21. Wu, J. et al. Achieving highly efficient, selective, and stable CO_2 reduction on nitrogen-doped carbon nanotubes. *ACS Nano* **9**, 5364–5371 (2015).
22. Liu, J. et al. Metal-free efficient photocatalyst for stable visible water splitting via a two-electron pathway. *Science* **347**, 970–974 (2015).
23. Wang, X., Chen, X., Thomas, A., Fu, X. & Antonietti, M. Metal-containing carbon nitride compounds: a new functional organic-metal hybrid material. *Adv. Mater.* **21**, 1609–1612 (2009).
24. Bhowmik, T., Kundu, M. K. & Barman, S. Palladium nanoparticle–graphitic carbon nitride porous synergistic catalyst for hydrogen evolution/oxidation reactions over a broad range of ph and correlation of its catalytic activity with measured hydrogen binding energy. *ACS Catal.* **6**, 1929–1941 (2016).
25. Gong, Y., Li, M., Li, H. & Wang, Y. Graphitic carbon nitride polymers: promising catalysts or catalyst supports for heterogeneous oxidation and hydrogenation. *Green Chem.* **17**, 715–736 (2015).
26. Balog, R. et al. Atomic hydrogen adsorbate structures on graphene. *J. Am. Chem. Soc.* **131**, 8744–8745 (2009).
27. Duplock, E. J., Scheffler, M. & Lindan, P. J. D. Hallmark of perfect graphene. *Phys. Rev. Lett.* **92**, 225502–225504 (2004).
28. Li, H. et al. Carbon dots from PEG for highly sensitive detection of levodopa. *J. Mater. Chem. B* **3**, 2378–2387 (2015).
29. Li, H. et al. Fluorescent N-doped carbon dots for both cellular imaging and highly-sensitive catechol detection. *Carbon* **91**, 66–75 (2015).
30. Guo, S. J. et al. Cu-CDots nanocorals as electrocatalyst for highly efficient CO_2 reduction to formate. *Nanoscale* **9**, 298–304 (2017).
31. Tang, D. et al. Carbon quantum dot/NiFe layered double-hydroxide composite as a highly efficient electrocatalyst for water oxidation. *ACS Appl. Mater. Interfaces* **6**, 7918–7925 (2014).
32. Li, H., Kang, Z., Liu, Y. & Lee, S. T. Carbon nanodots: synthesis, properties and applications. *J. Mater. Chem.* **22**, 24230–24253 (2012).
33. Wang, L. et al. Nitrogen-doped porous carbon/Co_3O_4 nanocomposites as anode materials for lithium-ion batteries. *ACS Appl. Mater. Interfaces* **6**, 7117–7125 (2014).
34. Ming, H. et al. Large scale electrochemical synthesis of high quality carbon nanodots and their photocatalytic property. *Dalton Trans.* **419**, 526–9531 (2012).
35. Chen, X. et al. Highly selective hydrogenation of furfural to furfuryl alcohol over Pt nanoparticles supported on g-C_3N_4 nanosheets catalysts in water. *Sci. Rep.* **6**, 28558–2871 (2016).
36. Abbas, M. A. & Bang, J. H. Rising again: opportunities and challenges for platinum-free electrocatalysts MoS_2 nanoparticles grown on graphene: an advanced catalyst for the hydrogen evolution reaction. *Chem. Mater.* **27**, 7218–7235 (2015).
37. Zhao, S. et al. Carbon quantum dots modified MoS_2 with visible-light-induced high hydrogen evolution catalytic ability. *Carbon* **99**, 599–606 (2016).
38. Liu, J. et al. Total photocatalysis conversion from cyclohexane to cyclohexanone by C_3N_4/Au nanocomposites. *Green Chem.* **16**, 4559–4565 (2014).

Author contributions

Z.K. designed and supervised the project. Y.L. partly designed and supervised the project. Y.L. and J.X. supervised parts of the project. S.G. conducted the synthesis. S.Z. performed the test of the electrochemical surface area. S.Z. and X.W. performed the BET measurements. S.G. carried out all remaining electrochemical measurements and the catalysts characterizations. S.G. wrote the manuscript. N.Y. contributed to the data analysis of the i–t curves in the CO_2-saturated $KHCO_3$ solution and the PB solution. Y.L. and Z.K. modified and finalized the manuscript. All authors contributed to data analysis and approved the final version of the manuscript.

Additional information

Competing interests: The authors declare no competing financial interests.

Reprints and permission information is available online at http://npg.nature.com/reprintsandpermissions/

Publisher's note: Springer Nature remains neutral with regard to jurisdictional claims in published maps and institutional affiliations.